Li–Mn–metal oxide nanoparticles synthesized by induction thermal plasmas for Li-ion batteries

H. Sone, S. Yoshida, T. Kageyama, M. Tanaka and T. Watanabe

Department of Chemical Engineering, Kyushu University, 744 Motooka, Nishi-ku, Fukuoka 819-0395, Japan

Abstract: Li–Mn–metal oxide nanoparticles were synthesized as the active materials of the positive electrodes of Li-ion batteries using induction thermal plasma. The crystal structures of the nanoparticles during the thermal plasma processing were examined in two different systems: Li–Mn–Ni–O and Li–Mn–Fe–O. In the Li–Mn–Ni–O system, NiO nucleated first, whereas in the Li–Mn–Fe–O system, MnO nucleated first. X-ray diffraction and transmission electron microscopy analyses showed that these systems were successfully synthesized in the $LiMn_{1.5}Ni_{0.5}O_4$ and $Li_2Mn_{1.5}Fe_{0.5}O_4$ nanoparticles.

Keywords: thermal plasma, Li–Mn–Fe oxide, Li–Mn–Ni oxide, lithium-ion battery

1. Introduction

Thermal plasma processing offers many advantages for producing nanomaterials, including high enthalpy, high chemical reactivity, choice of oxidizing or reducing atmosphere, and rapid quenching. Induction thermal plasma is characterized by long residence time of in-flight processing compared to other types of thermal plasmas. Moreover, many types of nanoparticles, including metals, oxides, borides, nitrides, carbides, and silicides can be synthesized using induction thermal plasma [1-4].

Currently, Li–Mn–metal oxide nanoparticles are used as the active material in the positive electrodes of Li-ion batteries. The chemical properties and characteristics of Li–Mn–metal oxide nanoparticles depend on the crystal structure. Therefore, control of the crystal structure during the synthesis process is important.

The effect of replacing a portion of Mn with Ni or Fe in spinel-structured Li–Mn–metal oxide nanoparticles on the electrochemical properties was investigated in this study. In addition, homogeneous nucleation mechanism of the Li–Mn–metal oxide nanoparticles was examined using thermal equilibrium considerations.

2. Experimental conditions

A schematic of the experimental apparatus used for the induction thermal plasma process is shown in Fig. 1. The apparatus mainly comprises a plasma torch to generate the plasma, a reaction chamber to synthesize nanoparticles, and a recovery section to recover the nanoparticles. The induction thermal plasma process is described as follows: raw materials in powdered form supplied together with a carrier gas are evaporated in the plasma torch; homogeneous nucleation occurs in the reaction chamber; and nanoparticles are formed via heterogeneous condensation.

The experimental frequency was 4 MHz, and the applied power was 20 kW. The experiments were conducted at atmospheric pressure with Ar as the carrier and inner gas and Ar and O_2 as the sheath gas. A mixed powder of Li_2CO_3, MnO_2, and Fe or Ni was used as the raw material,

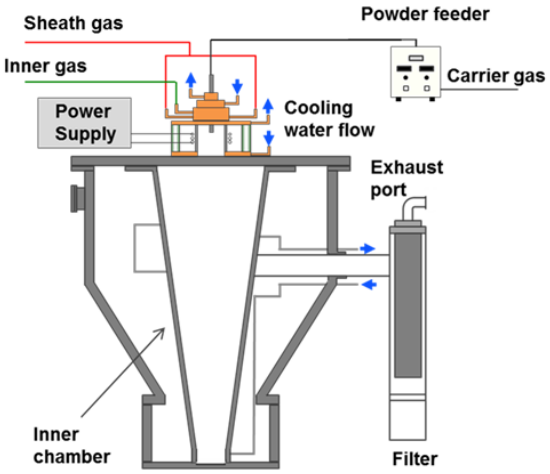

Fig. 1. Schematic of experimental setup for induction thermal plasma process.

and the powder was fed to the plasma at 300 mg/min. The composition of the raw material was Li:MnNi = 1:2 or Li:MnFe = 1:1. The crystalline structures of the nanoparticles were identified with powder X-ray diffraction (XRD), and the particle morphology and size distribution were evaluated using transmission electron microscopy (TEM).

3. Experimental results

The XRD patterns of the Li–Mn–Ni–O nanoparticles synthesized at O_2 gas flow rates 0, 2.5 and 5 L/min are shown in Fig. 2. The Li–Mn–Ni–O nanoparticles had the same crystal structure as spinel-type $LiMn_{1.5}Ni_{0.5}O_4$ at all tested O_2 flow rates. The Li–Ni oxide nanoparticles with a cubic rock-salt structure were synthesized when only Ar was used as the sheath gas. In contrast, $LiMn_{1.5}Ni_{0.5}O_4$ nanoparticles with the spinel structure were synthesized when O_2 was added to the sheath gas. The intensities of the Li–Ni oxide and Mn_3O_4 peak decreased, and the peak

corresponding to the (111) plane of $LiMn_{1.5}Ni_{0.5}O_4$ at 19 degrees appeared instead when O_2 was used as the sheath gas at a flow rate of 2.5 L/min. This peak at 19 degrees became stronger and sharper when the flow rate of O_2 as the sheath gas increased to 5 L/min. This suggests that increasing the O_2 gas flow rate enhances the production of $LiMn_{1.5}Ni_{0.5}O_4$. The intensity of the $LiMn_{1.5}Ni_{0.5}O_4$ peaks increased when that of the Li–Ni oxide peak decreased. Thus, the crystalline structures of the particles switched from an Li-Ni oxide structure to a $LiMn_{1.5}Ni_{0.5}O_4$ structure as the flow rate of O_2 increased. The XRD patterns suggest that the crystalline structure changed from a cubic rock-salt structure to a spinel structure with increasing O_2 flow rate.

The XRD patterns of the synthesized $Li_2Mn_{1.5}Fe_{0.5}O_4$ nanoparticles at O_2 gas flow rates 0, 2.5, and 5 L/min are shown in Fig. 3. The $Li_2Mn_{1.5}Fe_{0.5}O_4$ nanoparticles had the same spinel-type crystal structures as the $LiMn_{1.5}Ni_{0.5}O_4$ nanoparticles at all tested O_2 flow rates. The Li–Fe oxide nanoparticles with a cubic rock-salt structure were synthesized when only Ar was used as the sheath gas. $Li_2Mn_{1.5}Fe_{0.5}O_4$ nanoparticles with the spinel structure were synthesized when O_2 was added to the sheath gas. When O_2 was used as the sheath gas at a flow rate of 2.5 L/min, the intensity of the peak corresponding to the (400) plane of Li-Fe oxide at 42 degrees decreased, and a peak corresponding to the (111) plane of $Li_2Mn_{1.5}Fe_{0.5}O_4$ at 19 degrees appeared. The intensity of the $Li_2Mn_{1.5}Fe_{0.5}O_4$ peak increased as that of the Li-Fe oxide and Mn_3O_4 peak decreased. Thus, the structures of the particles switched from a Li-Fe oxide crystalline structure to a $Li_2Mn_{1.5}Fe_{0.5}O_4$ structure as the flow rate of O_2 increased. The XRD patterns suggest that the crystalline structure changed from a cubic rock-salt structure to a spinel structure with increasing O_2 flow rate. Unlike for $LiMn_{1.5}Ni_{0.5}O_4$, the $Li_2Mn_{1.5}Fe_{0.5}O_4$ peak did not change when the flow rate of O_2 as the sheath gas increased to 5 L/min. This is attributed to the fact that the Li content in the Li–Mn–Fe–O system is higher than in the Li–Mn–Ni–O system, whereas the oxygen content in the Li–Mn–Fe–O system is smaller.

The particle size distributions were determined from the TEM observation of approximately 200 different particles. The average particle sizes for the Li-Mn-Ni-O and Li-Mn-Fe-O systems were 60.2 and 65.2 nm, respectively. The synthesized nanoparticles had polygonal structures peculiar for the spinel structure. The nanoparticles had tetradecahedral crystalline structure comprised of (111) planes × eight faces for the hexagon and (100) planes × six faces for the tetrahedron.

The energy-dispersive X-ray spectroscopy (EDS) results for different raw material compositions (Li:Mn:Ni = 1:1.5:0.5, O_2 flow rate = 2.5 L/min and Li:Mn:Fe = 1:0.75:0.25, O_2 flow rate = 2.5 L/min) are shown in Fig. 5. All the observed Li-Mn-Ni-O nanoparticles contained both Mn and Ni. Similarly, all observed Li-Mn-Fe-O nanoparticles contained both Mn and Fe. These results suggest that the Li-Mn-Ni-O and Li-Mn-Fe-O nanoparticles were spinel-type $LiMn_{1.5}Ni_{0.5}O_4$ and

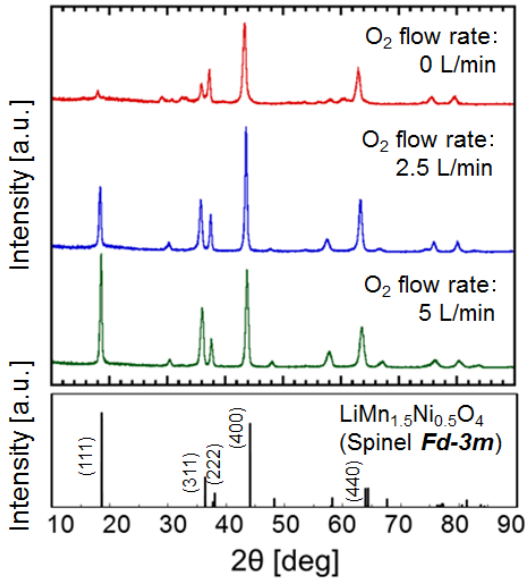

Fig. 2. XRD spectra of synthesized nanoparticles in Li–Mn–Ni–O system.

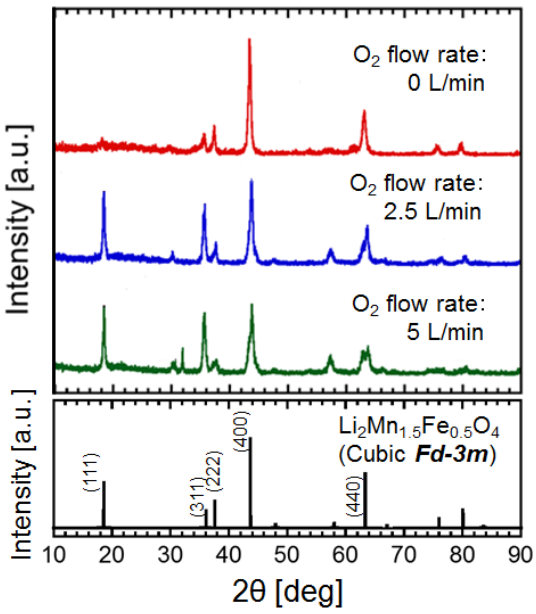

Fig. 3. XRD spectra of synthesized nanoparticles in Li–Mn–Fe–O system.

$Li_2Mn_{1.5}Fe_{0.5}O_4$ nanoparticles, respectively.

Electron diffraction analysis indicated the synthesis of additional products, $Li_{0.4}Ni_{1.6}O_2$ (Fm-3m) and $LiMnO_2$ (Pnma), without O_2 addition. $LiMn_{1.5}Ni_{0.5}O_4$ (Fd-3m) was produced in all samples when the O_2 flow rate was 5 L/min. The electron diffraction results are consistent with the XRD patterns, which indicated that $LiMn_{1.5}Ni_{0.5}O_4$ was synthesized. Additional products, $LiFeO_2$ (Fm-3m) and Fe_3O_4 (Fd-3m), were also synthesized in the Li-Mn-Fe-O system without O_2 addition. $Li_2Mn_{1.5}Fe_{0.5}O_4$ (Fd-3m) was produced at the O_2 flow rate of 2.5 L/min. These electron diffraction results are consistent with the XRD patterns,

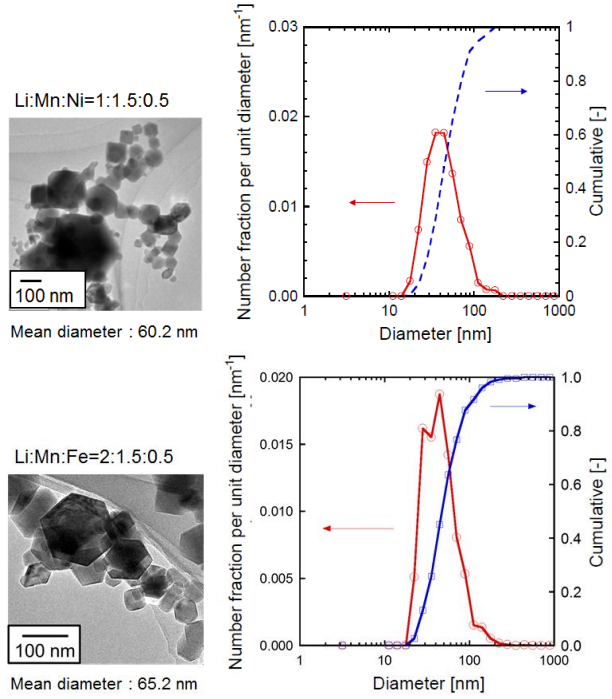

Fig. 4. Particle size distribution of $LiMn_{1.5}Ni_{0.5}O_4$ and $Li_2Mn_{1.5}Fe_{0.5}O_4$ nanoparticles at O_2 2.5 L/min.

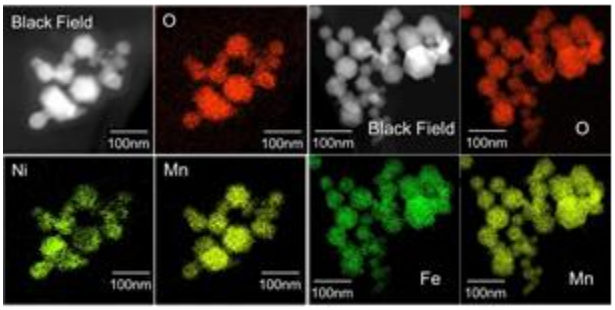

Fig. 5. TEM-EDS images of synthesized nanoparticles of the Li–Mn–Ni–O and Li–Mn–Fe–O systems.

which indicated that $Li_2Mn_{1.5}Fe_{0.5}O_4$ was synthesized.

The diffraction patterns of the nanoparticles of the Li–Mn–Ni–O and Li–Mn–Fe–O systems were interpreted on the basis of nucleation theory [5-7] and thermodynamic considerations. Figure 6 shows the nucleation temperature of the Li–Mn–Ni–O and Li–Mn–Fe–O systems. Figure 7 shows the Gibbs free-energy change of the Li–Mn–Ni–O and Li–Mn–Fe–O systems. The homogeneous nucleation temperature was estimated on the basis of the homogeneous nucleation rate to investigate the process of forming $LiMn_{1.5}Ni_{0.5}O_4$ and $Li_2Mn_{1.5}Fe_{0.5}O_4$ nanoparticles in induction thermal plasmas. The vapor generated in the thermal plasma is quenched as it flows downstream. Because the saturated vapor pressure of the raw material decreases rapidly, homogeneous nucleation occurs with supersaturation as the driving force. The saturation ratio is defined as

$$S = \frac{P}{P_s}, \tag{1}$$

where S is the saturation ratio, P is the partial pressure of the vapor species, and P_s is the equilibrium vapor pressure. Many different equations were previously proposed to describe the homogeneous nucleation rate. In a thermal plasma, the following equation based on the classical theory of Girshick and coworkers [8, 9] is often used:

$$J = \frac{\beta_{ij} n_s^2 S}{12}\sqrt{\frac{\Theta}{2\pi}}\exp\left[\Theta - \frac{4\Theta^3}{27(\ln S)^2}\right], \tag{2}$$

where J (m^{-3} s^{-1}) is the nucleation rate, n_s (m^{-3}) is the number density under equilibrium vapor pressure, and Θ is the dimensionless surface tension, which depends only on the temperature and physical properties of molecules. The parameter Θ is expressed as

$$\Theta = \frac{\sigma s_1}{kT}, \tag{3}$$

where σ (N/m) is the surface tension, s_1 (m^2) is the surface area of a monomer particle, and k (J/K) is the Boltzmann constant. Homogeneous nucleation starts when the supersaturation is >1. Since the production and evaporation rates of a particle are large at a low supersaturation level, the generated nucleus is usstable. When the supersaturation is ≥1, a nucleus is generated.

$$\beta_{ij} = \left(\frac{3v_1}{4\pi}\right)^{1/6}\sqrt{\frac{6kT}{\rho_p}\left(\frac{1}{i}+\frac{1}{j}\right)}\times\left(i^{1/3}+j^{1/3}\right)^2. \tag{4}$$

where v_1 is the volume of the monomer particle and ρ_p is the density of the monomer. Here, collision between the molecules occurs when $i = j = 1$. It was experimentally demonstrated that stable nucleation begins when the homogeneous nucleation rate is 1 cm^{-3} s^{-1}, and the corresponding temperature is the nucleation temperature [9].

These nucleation discussion reveals that NiO nucleated first in the Li–Mn–Ni–O system, whereas MnO nucleated first in the Li–Mn–Fe–O system. For Li–Mn–Ni–O system, formation of $LiMn_2O_4$ is the dominant reaction due to lower ΔG of $LiMn_2O_4$ than that of $LiNiO_2$ [10]. Similarly, for Li–Mn–Fe–O system, $LiMn_2O_4$ is the dominant reaction. The spinel-type Li-Mn-Fe-O system is formed on the basis of $LiMn_2O_4$, the most stable compound in the Li-Mn system.

Electrochemical characteristics were confirmed by current-voltage characteristics. The measured current-voltage characteristics of $LiMn_{1.5}Ni_{0.5}O_4$ nanoparticles are peculiar for nanoparticles. $LiMn_{1.5}Ni_{0.5}O_4$ showed reaction patterns peculiar for those of Ni at around 4.7 V, and the conductivity of trivalent tetravalent Mn was confirmed by hopping conduction. The reaction from 4 to 5 V of peculiar to Ni is expressed as

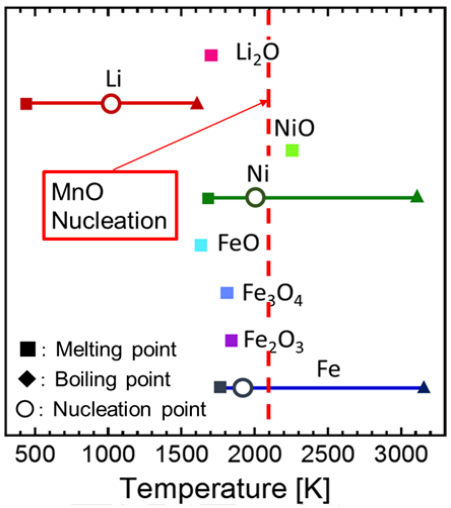

Fig. 6. Nucleation, boiling, and melting temperatures for $LiMn_2O_4$, $LiNiO_2$,of Mn, Ni, Fe, Li, and their oxides.

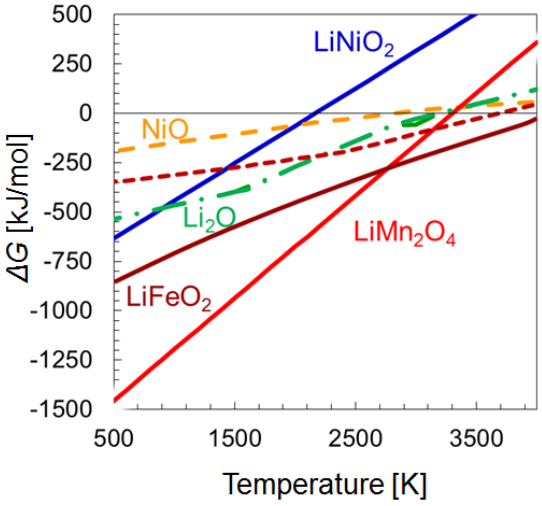

Fig. 7. Gibbs free-energy change for $LiMn_2O_4$, $LiNiO_2$, $LiFeO_2$, MnO, NiO, and Li_2O.

$$\begin{aligned} &Li[Ni(II)_{0.5}Mn(IV)_{1.5}]O_4 \\ &\rightarrow Li_{0.5}[Ni(III)_{0.5}Mn(IV)_{1.5}]O_4 + 0.5Li^+ + 0.5e^- \cdot \\ &\rightarrow Li_{0.5}[Ni(IV)_{0.5}Mn(IV)_{1.5}]O_4 + 0.5Li^+ + 0.5e^- \end{aligned} \quad (5)$$

Similarly, the conductivity of trivalent tetravalent Mn was confirmed in $Li_2Mn_{1.5}Fe_{0.5}O_4$ by hopping conduction. The reaction from 3.5 to 5 V for Mn and Fe is expressed as

$$\begin{aligned} &Li_2[Fe(III)_{0.5}Mn(III)_{1.5}]O_4 \\ &\rightarrow Li_{0.5}[Fe(III)_{0.5}Mn(IV)_{1.5}]O_4 + 1.5Li^+ + 1.5e^- \cdot \\ &\rightarrow [Fe(IV)_{0.5}Mn(IV)_{1.5}]O_4 + 0.5Li^+ + 0.5e^- \end{aligned} \quad (6)$$

Therefore, the synthesized $LiMn_{1.5}Ni_{0.5}O_4$ and $Li_2Mn_{1.5}Fe_{0.5}O_4$ nanoparticles were revealed to be nanoparticles possessing electrical conductivity.

4. Conclusion

The crystal structures of Li–Mn–metal oxide nanoparticles in this study suggest that the nanoparticles can be controlled by replacing a portion of Mn with Ni or Fe during synthesis in induction thermal plasmas. Furthermore, Li–Mn–metal oxide can be controlled by adjusting the partial pressure of O_2.

In the formation mechanism, the Li–Mn–metal oxide is formed by first nucleating the oxide at a high nucleation temperature and then condensing the nucleated oxide. Thermodynamically stable Mn-oxides are produced ($\Delta G_{\text{Li-Metal-oxide}} > \Delta G_{\text{Metal-oxide}}$) at a low O_2 partial pressure. In contrast, thermodynamically stable spinel type Li–Mn oxide is produced ($\Delta G_{\text{Spinel}} < \Delta G_{\text{Layered}}$) at a high O_2 partial pressure. The electron conductivity of synthesized crystal structure was improved by electron hopping of Mn.

5. References

[1] M. Shigeta, T. Watanabe, J. Mater. Res. **20** 2801 (2005).

[2] M. Shigeta, T. Watanabe, J. Appl. Phys. **103**, 074913 (2008).

[3] M. Tanaka, J. Noda, T. Watanabe, J. Matsuno, A. Tsuchiyama, J. Phys. Conf. Ser. **518**, 012025 (2014).

[4] Y. Cheng, M. Tanaka, T. Watanabe, S. Y. Choi, M.S. Shin, J. Phys. Conf. Ser. **518**, 012026 (2014).

[5] T. Watanabe, H. Itoh, Y. Ishii, Thin Solid Films **390** 44 (2001).

[6] T. Watanabe, H. Okumiya, Sci. Technol. Adv. Mater **5** 639 (2004).

[7] M. Tanaka, T. Kageyama, H. Sone, S. Yoshida, D. Okamoto, T. Watanabe, Nanomater. **6**, 60 (2016).

[8] S.L. Girshick C.P. Chiu, J. Chem. Phys. **93**, 1273 (1990).

[9] S.L. Girshick, C.P. Chiu, P. H. McMurry, Aerosol Sci. Technol. 13, 465 (1990).

[10] S.K. Friedlander, Smoke, Dust, and Haze: Fundamentals of Aerosol Dynamics (Oxford University Press, Oxford, UK, 2000) 2nd ed., p. 407.

[11] H. Sone, T. Kageyama, M. Tanaka, and T. Watanabe, Jpn. J. Appl. Phys. **55**, 07LE04 (2016).